




On the 3D transport of galactic cosmic rays in a selection of exoplanet-hosting astrospheres: the influence of stellar rotation

Juandrè Light ¹★, N. Eugene Engelbrecht,¹ Konstantin Herbst ^{2,3} and K. D. Scherer ⁴

¹Center for Space Research, North-West University, Potchefstroom 2520, South Africa

²Institute of Planetary Research, German Aerospace Center (DLR), D-12489 Berlin, Germany

³Centre for Planetary Habitability (PHAB), Department of Geosciences, University of Oslo, 0316 Oslo, Norway

⁴Institut für Theoretische Physik IV: Weltraum- und Astrophysik, Ruhr-Universität Bochum, 44780 Bochum, Germany

Accepted 2025 January 20. Received 2025 January 18; in original form 2024 September 20

ABSTRACT

Galactic cosmic rays (GCRs) may influence the habitability of exoplanets. The recently proposed relationship between GCR intensities at exoplanetary locations and the rotation periods of their host stars is here investigated for several M-dwarf astrospheres, namely Proxima Centauri, TRAPPIST-1, GJ 436, and LHS1140, using a three-dimensional GCR modulation code. This relation, where higher GCR intensities result from enhanced particle transport along astrospheric magnetic fields that are underwound due to longer stellar rotation periods, is found to hold for the astrospheres considered here. The influence of the stellar rotation period on GCR intensities in a Sun-like astrosphere on Earth and Mars-like atmospheres is also investigated and found to directly influence atmospheric ionization and radiation exposure.

Key words: MHD – planetary systems – stars: winds, outflows – cosmic rays.

1 INTRODUCTION

Galactic cosmic rays (GCRs) may reasonably be expected to have an influence on the habitability of exoplanets in astrospheres (see e.g. Herbst et al. 2022, and references therein). This effect, however, is not necessarily straightforward to quantify, as the modelling of the transport of these particles in astrospheres, in order to determine the intensities that would be expected at exoplanet locations, requires knowledge of the large and small-scale astrospheric and stellar parameters. This information is often not available from observations, or is very limited, and therefore such transport studies often rely on the results of magnetohydrodynamic (MHD) simulations of the astrospheric plasma environments (for some examples of such MHD simulations, see e.g. Vidotto et al. 2011; Rogers & Showman 2014; Mackey, Green & Moutzouri 2021; Meyer et al. 2021; Baalman et al. 2022; Herbst et al. 2022).¹ As such, several studies have modelled GCR intensities within exoplanet-hosting astrospheres, and, while two of these studies suggest that GCR intensities may be larger than intensities at Earth (Herbst et al. 2020b; Engelbrecht et al. 2024), other studies argue that the intensities are significantly lower, that is to say very strongly modulated (e.g. Sadovskii, Struminsky & Belov 2018; Mesquita, Rodgers-Lee & Vidotto 2021; Mesquita et al. 2022). These studies mostly (with the exception of Engelbrecht et al. 2024) rely on solving a one-dimensional (1D) Parker (1965) GCR transport

equation (TPE), with Sadovskii et al. (2018) using a force-field solution (Gleeson & Axford 1968) of said equation. Differences in the GCR intensities reported in the above-mentioned 1D modulation studies may be due to the differences in model input parameters (such as stellar wind speeds and magnetic fields) used in those studies. However, the 1D and force field solutions have limitations in that they are unable to realistically model the complex three-dimensional (3D) physical transport mechanisms governing the transport of GCRs (e.g. Engelbrecht & Di Felice 2020; Engelbrecht et al. 2022a), and cannot take into account the observed and modelled 3D structures of the astrospheres in question. For example, such lower-dimensional approaches are simply unable to model the inherently 3D process of particle drifts due to curvatures in, and gradients of, the 3D astrospheric magnetic field (AMF), which have long been known to influence GCR transport in the heliosphere (see e.g. Jokipii, Levy & Hubbard 1977; Jokipii & Thomas 1981; Kota & Jokipii 1983; Potgieter & Burger 1990), where, during positive magnetic polarity cycle periods where the heliospheric magnetic field (HMF) is directed outwards in the Northern hemisphere (and inwards in the Southern hemisphere), positively charged particles drift inwards from over the polar regions, and out along the heliospheric current sheet. These particles then drift in the opposite directions during negative polarity cycles, when the directions of the HMF are reversed in the Northern and Southern hemispheres (see also Reinecke & Potgieter 1994; Mohlolo, Engelbrecht & Ferreira 2022). The 1D modelling approach has also been shown to potentially lead to overestimations as to the potential significance of different transport mechanisms: Light et al. (2022), when studying the modulation of GCRs with a 1D GCR modulation code in the astrosphere of a luminous blue variable star found that the particles underwent unusually high levels of

* E-mail: juandrelight@gmail.com

¹Note that not all these simulations are for the winds from low-mass stars, and that the physics behind the wind-driving mechanism can be different for different types of stars.

diffusive shock acceleration due to the fact that they became trapped near travelling shocks. Those authors conclude that this trapping might not necessarily occur if a 3D transport model were employed, as particles would then have been able to escape said shocks via diffusion parallel to the astrospheric magnetic field, or through drift. The force-field approach in itself is also very restrictive due to the unphysical assumptions made in its derivation, as it assumes a 1D, spherically symmetric system and contains no adiabatic energy changes (Caballero-Lopez & Moraal 2004). This limits its usefulness in terms of prediction and extrapolation to astrospheric modulation studies (Engelbrecht & Di Felice 2020). In order to model the transport of GCRs more physically, a 3D approach is thus required, as this will allow the modelling of the inherently 3D mechanisms governing GCR transport to be done in a more realistic manner. In brief, model plasma input parameters may vary, but their influence on GCR modulation can only be self-consistently modelled in 3D.

Engelbrecht et al. (2024) performed the first 3D study of the transport of GCRs for one such astrosphere, namely that of Proxima Centauri. They reported that GCR intensities at Proxima Centauri b, a rocky, possibly Earth-like planet at a distance of 0.0485 au from its star (well within the habitable zone, see e.g. Anglada-Escudé et al. 2016; Hill et al. 2023), were considerably larger than those reported by previous studies (e.g. Sadovski et al. 2018; Mesquita et al. 2021; Mesquita et al. 2022). This is due to the fact that, because of its significantly slower rotation rate than the Sun, the AMF of Proxima Centauri would be considerably underwound relative to the HMF, assuming that it can be described by the standard Parker (1958) spiral field, as is attested by MHD simulations (e.g. Herbst et al. 2020b). Such an underwound field would allow GCRs to enter the astrosphere more effectively by means of diffusion parallel to the AMF. This is in contrast to the perpendicular diffusion-dominated radial transport of GCRs in the heliosphere, and is more effective, as perpendicular diffusion coefficients can typically (for heliospheric conditions) be several orders of magnitude smaller than parallel diffusion coefficients (see e.g. Engelbrecht et al. 2022a). This raises the intriguing possibility that the influence of GCRs on an exoplanetary atmosphere, or even its habitability, could be directly related to the rotation period of its host star. The present study aims to investigate this by following the modelling approach of Engelbrecht et al. (2024), namely utilizing a fully 3D stochastic solver of the Parker TPE that has also been successfully used in the heliosphere (see e.g. Engelbrecht & Burger 2015; Moloto, Engelbrecht & Burger 2018; Engelbrecht 2019; Engelbrecht & Moloto 2021) to compute GCR intensities at the locations of several known exoplanets, hosted by several very different astrospheres, namely those of Proxima Centauri, TRAPPIST-1, GJ 436, and LHS 1140 (see Section 3). As full MHD simulations of some of these astrospheres are not yet available, large and small-scale plasma parameters will be modelled following theoretically and observationally motivated approaches long used in heliospheric studies of GCR transport, as outlined for the astrosphere of Proxima Centauri by Engelbrecht et al. (2024), modified to conform to the results of published astrospherical observations and simulations where possible. Studying these different astrospheres, which have differing stellar parameters, we will show that the stellar rotation rate has a significant effect on the transport of the GCRs for a variety of astrospheric conditions through the influence it has on the 3D AMF geometry and may thus provide a further potential constraint on the habitability of exoplanets.

As discussed in, e.g. Herbst et al. (2019b, 2020b, 2024), cosmic rays influence (exo)planetary atmospheres, leading to changes in the atmospheric chemistry and climate, and with that on potential biosignatures such as ozone and methane, particularly in the case

of Earth-like (i.e. N_2 - O_2 dominated) atmospheres. Thus, it is of uttermost importance to include cosmic ray studies when it comes to understanding and interpreting existing *JWST* (e.g. Gardner et al. 2006, 2023) observations and future Atmospheric Remote-sensing Exoplanet Large-survey (ARIEL; e.g. Tinetti et al. 2022) transmission spectra. Note that the chemistry of other exoplanetary atmospheres is also impacted by CRs. For a discussion on the impact on hot Jupiters the reader is referred to Barth et al. (2021). It is further known that cosmic rays can drive the formation of prebiotic molecules (see e.g. Rimmer, Helling & Bilger 2014), the building blocks of life. However, an enhanced flux of these energetic particles within an exoplanetary atmosphere can lead to enhanced radiation exposure and, with that, can induce DNA damage (see e.g. Kennedy 2014). There are even indications that particularly GCRs have indirectly influenced the helicity of DNA (Globus & Blandford 2020). Thus, the manifold effects of cosmic rays within (exo)planetary atmospheres cannot be neglected in the context of (exo)planetary habitability.

The following section provides detail as to the 3D numerical GCR modulation employed, detailing the diffusion coefficients used (Section 2.1) and heliospheric versus astrospheric plasma parameters (Section 2.2), the former of which being employed in a validation of the model for heliospheric conditions (Section 2.3). Subsequently, in Section 3, observed and MHD-simulated plasma parameters for several astrospheres are discussed, and motivated as inputs for the modulation code. The resulting differential intensities, computed at the locations of the exoplanets contained within these astrospheres, are presented in Section 4, with a particular emphasis on the influence of stellar rotation period on computed intensities. The resulting effects on atmospheric ionization, for both an Earth-like and a Mars-like atmosphere, are explored in Section 5. The paper closes with a summary and discussion of the results of this study.

2 NUMERICAL MODEL

The transport of cosmic rays (CRs) is described by the Parker (1965) TPE, which, in the absence of sinks and/or sources of energetic particles, is given by

$$\frac{\partial f}{\partial t} = \nabla \cdot (\mathbf{K} \cdot \nabla f) - \mathbf{V}_{sw} \cdot \nabla f + \frac{1}{3} (\nabla \cdot \mathbf{V}_{sw}) \frac{\partial f}{\partial \ln p}, \quad (1)$$

where $f(\mathbf{r}, p, t)$ is the omnidirectional CR phase-space density, as a function of position \mathbf{r} , momentum p and time t , which is related to the CR differential intensity (DI) by $j_T = p^2 f$ (see e.g. Moraal 2013). The TPE describes the diffusion and drift of CRs through the 3D diffusion tensor \mathbf{K} . The outward convection of CRs with the stellar wind is described by the term $\mathbf{V}_{sw} \cdot \nabla f$, and adiabatic energy changes by the term $1/3 (\nabla \cdot \mathbf{V}_{sw}) \partial f / \partial \ln p$. It is useful to write the 3D diffusion tensor \mathbf{K} in AMF aligned coordinates such that (see e.g. Burger et al. 2008)

$$\mathbf{K}' = \begin{bmatrix} \kappa_{\perp,3} & \kappa_A & 0 \\ -\kappa_A & \kappa_{\perp,2} & 0 \\ 0 & 0 & \kappa_{\parallel} \end{bmatrix} \quad (2)$$

where \mathbf{K}' is written in terms of diffusion coefficients perpendicular and parallel to the AMF, which can be related to the corresponding mean free paths (MFPs) via, e.g. $\kappa_{\perp,\parallel} = v \lambda_{\perp,\parallel} / 3$ (Shalchi 2009), where the particle speed is denoted by v . These elements and the off-diagonal elements representing drift coefficients are discussed in more detail in Section 2.1.

The Parker TPE is solved here using a stochastic differential equation (SDE) approach as presented in Engelbrecht & Burger (2015). Here, we follow the same approach as what was done by Engelbrecht et al. (2024). The SDE approach involves writing the Parker TPE as a set of equivalent Itô-type SDE equations (see e.g. Zhang 1999; Strauss & Effenberger 2017):

$$dx_i = A_i(x_i)dt + \sum_j B_{i,j}(x_i) \cdot dW_i, \quad (3)$$

where i represents the three spherical coordinates, r , θ , ϕ , and energy E . For a generalized 3D AMF, the components of the tensor $\mathbf{B}_{i,j}$ are given by (Pei et al. 2010; Engelbrecht & Burger 2015)

$$\begin{aligned} B_{1,1} &= \frac{\sqrt{2(\kappa_{\phi\phi}\kappa_{r\theta}^2 - 2\kappa_{r\phi}\kappa_{r\theta}\kappa_{\theta\phi} + \kappa_{rr}\kappa_{\theta\phi}^2 + \kappa_{\theta\theta}\kappa_{r\phi}^2 - \kappa_{rr}\kappa_{\theta\theta}\kappa_{\phi\phi})}}{\sqrt{\kappa_{\theta\phi}^2 - \kappa_{\theta\theta}\kappa_{\phi\phi}}}, \\ B_{1,2} &= \frac{\kappa_{r\phi}\kappa_{\theta\phi} - \kappa_{r\theta}\kappa_{\phi\phi}}{\kappa_{\theta\phi}^2 - \kappa_{\theta\theta}\kappa_{\phi\phi}} \sqrt{2\left(\kappa_{\theta\theta} - \frac{\kappa_{\theta\phi}^2}{\kappa_{\phi\phi}}\right)}, \\ B_{1,3} &= \frac{\sqrt{2\kappa_{r\phi}}}{\sqrt{\kappa_{\phi\phi}}}, \\ B_{2,2} &= \frac{\sqrt{2(\kappa_{\theta\theta} - \kappa_{\theta\phi}^2/\kappa_{\phi\phi})}}{r}, \\ B_{2,3} &= \frac{\kappa_{\theta\phi}}{r} \sqrt{\frac{2}{\kappa_{\phi\phi}}}, \\ B_{3,3} &= \frac{\sqrt{2\kappa_{\phi\phi}}}{r \sin \theta}, \\ B_{2,1} &= B_{3,1} = B_{3,2} = 0 \end{aligned} \quad (4)$$

with the various κ values denoting elements of the diffusion tensor in spherical coordinates (which can be found in Burger et al. 2008). The components of the vector \mathbf{A} are given as (Engelbrecht & Burger 2015)

$$\begin{aligned} A_r &= \frac{1}{r^2} \frac{\partial}{\partial r} r^2 \kappa_{rr} + \frac{1}{r \sin \theta} \frac{\partial}{\partial \phi} \kappa_{r\phi} + \frac{1}{r \sin \theta} \frac{\partial}{\partial \theta} \kappa_{r\theta} \sin \theta \\ &\quad - V_{sw,r} - V_{d,r}, \\ A_\theta &= \frac{1}{r^2} \frac{\partial}{\partial r} r^2 \kappa_{r\theta} + \frac{1}{r^2 \sin \theta} \frac{\partial}{\partial \theta} \kappa_{\theta\theta} \sin \theta + \frac{1}{r^2 \sin \theta} \frac{\partial}{\partial \phi} \kappa_{\theta\phi} \\ &\quad - \frac{(V_{sw,\theta} + V_{d,\theta})}{r}, \\ A_\phi &= \frac{1}{r^2 \sin^2 \theta} \frac{\partial}{\partial \phi} \kappa_{\phi\phi} + \frac{1}{r^2 \sin^2 \theta} \frac{\partial}{\partial r} r \kappa_{r\phi} + \frac{1}{r^2 \sin^2 \theta} \frac{\partial}{\partial \theta} \kappa_{\theta\phi} \\ &\quad - \frac{(V_{sw,\phi} + V_{d,\phi})}{r \sin \theta}, \\ A_E &= \frac{1}{3} (\nabla \cdot \mathbf{V}_{sw}) \frac{(E + 2E_o)}{E + E_o} E. \end{aligned} \quad (5)$$

Note that the signs of the drift velocity $\mathbf{V}_d = \nabla \times \kappa_A \hat{e}_B$ [with \hat{e}_B an unit vector in the direction of the AMF, see Jokipii et al. (1977)] and stellar wind velocity \mathbf{V}_{sw} are reversed to explicitly show the time-backward manner within which the equations are solved.

A Wiener process is introduced through W_i where $dW_i = \eta(t)\sqrt{dt}$ and $\eta(t) \in (0, 1)$ represents a pseudo-random number, which is Gaussian distributed and generated using the Mersenne Twister algorithm. The above equations are solved in a time-backward manner for $N = 10^5$ pseudo-particles from the location of the respective exoplanets until they reach a specified boundary where

an average CR intensity is calculated using (Strauss et al. 2011)

$$j(x_i^o, t^o) = \frac{1}{N} \sum_{k=1}^N j_B(x_{i,k}^e, t_k^e), \quad (6)$$

with the boundary spectrum given by j_B , and superscript e denoting an exit time or position. This boundary could be a local interstellar spectrum (LIS) or a boundary spectrum at some pre-determined location. For more detailed discussion of the stochastic approach to solving the Parker equation, the works of Zhang (1999), Strauss & Effenberger (2017), and Moloto et al. (2019) can be consulted.

In this study, the boundary spectrum will be placed at the termination shocks (TSs) of the respective astrospheres. This allows for the use of an analytical description of the large-scale plasma parameters much like what is commonly done in heliospheric GCR modulation studies (see e.g. Potgieter 2013; Engelbrecht et al. 2022a), discussed in Section 2.2. The GCR proton boundary spectrum used in this study is the spectrum constructed by Moloto & Engelbrecht (2020) to agree with *Voyager* observations of intensities at 85 au as reported by Webber et al. (2008) within the heliosphere. This boundary spectrum is used as a first approach to the intensities at the TS of other astrospheres and is given by

$$j_B = \frac{17.0(P/P_0)^{-2.4}}{2.2 + 2.1(P/P_0)^{-3}}, \quad (7)$$

which is given in units of $m^2 s^{-1} sr^{-1} MeV^{-1}$, P the rigidity in GV, and $P_0 = 1$ GV. Although this spectrum may be an overestimate (especially at lower energies where modulation effects could be expected to play a more significant role), as the heliosheath differs from other astrosheaths, a full LIS will potentially be an even greater overestimate given the observed high amount of modulation in the heliosheath (e.g. Stone et al. 2013).

2.1 Diffusion coefficients

The choice of diffusion coefficients of CRs parallel and perpendicular to the AMF in this study follows the same approach taken by Engelbrecht et al. (2024) for Proxima Centauri. These diffusion coefficients were chosen as they have been used successfully in heliospheric GCR modulation studies (Engelbrecht et al. 2022a). Note that these coefficients, derived from first principles, are functions of various turbulence quantities which will be briefly introduced below. For more detailed information on these quantities, the interested reader is invited to consult, e.g. Matthaeus & Goldstein (1982), Frisch (1995), Matthaeus et al. (2007), Bruno & Carbone (2013), and Oughton & Engelbrecht (2021).

A parallel (to the AMF) MFP expression derived by Teufel & Schlickeiser (2003) from the Jokipii (1966) quasi-linear theory (QLT) is used, derived assuming a slab turbulence power spectrum with a wavenumber-independent energy-containing range and an inertial range with spectral index s , and is given by (Burger et al. 2008),

$$\lambda_{\parallel} = \frac{3s}{(s-1)} \frac{R^2}{k_m} \frac{B_0^2}{\delta B_{sl}^2} \left[\frac{1}{4\pi} + \frac{2R^{-s}}{\pi(2-s)(4-s)} \right], \quad (8)$$

where $s = 5/3$ (Kolmogorov 1941) and $R = R_L k_m$, making the parallel MFP expression a function of the maximal proton Larmor radius, R_L . The parallel MFP also depends on the wavenumber at which the slab spectrum inertial range commences, $k_m = 1/\lambda_{sl}$. The background magnetic field is given by B_0 , while δB_{sl}^2 denotes the slab variance, the mean square amplitude of the slab turbulent fluctuations. For more information of the slab [and two-dimensional (2D)] models of turbulence, see Matthaeus, Goldstein & Roberts

(1990); Bieber, Wanner & Matthaeus (1996); Forsyth et al. (1996); Bruno & Carbone (2013).

The perpendicular (to the AMF) MFP is obtained from the Nonlinear Guiding Center (NLGC) results of Shalchi, Bieber & Matthaeus (2004), derived for the same turbulence spectral form as the parallel MFP, as modified by Burger et al. (2008) to accommodate a general ratio of the slab to 2D energies (see e.g. Bieber et al. 1996; Oughton et al. 2015). This is given by

$$\lambda_{\perp} = \left[\alpha^2 \sqrt{3\pi} \frac{2\nu - 1}{\nu} \frac{\Gamma(\nu)}{\Gamma(\nu - 1/2)} \lambda_{2D} \frac{\delta B_{2D}^2}{B_0^2} \right]^{2/3} \lambda_{\parallel}^{1/3}, \quad (9)$$

where $\nu = s/2 = 5/6$ denotes half the Kolmogorov inertial range spectral index, and it is assumed that $\alpha^2 = 1/3$ (from numerical test-particle simulations by Matthaeus et al. 2003). For comprehensive reviews on the theory of diffusion in the presence of space plasma turbulence, see Shalchi (2009), Shalchi (2020), and Engelbrecht et al. (2022a). The perpendicular MFP is dependent on the 2D variance, δB_{2D}^2 , and the turnover scale where the inertial range begins on the assumed 2D turbulence power spectrum, λ_{2D} . The turbulence quantities in the above expressions are modelled following the approach of Engelbrecht et al. (2024), namely by assuming simple power-law scalings motivated by heliospheric observations, and scaled according to the relative strengths of the heliospheric to astrospheric magnetic fields (see Section 2.2 and equations 14 and 15).

Apart from diffusion parallel and perpendicular, GCRs can also drift due to gradients and curvatures in the AMF, as well as along any potential astrospheric current sheet (ACS; for discussions of this in the heliospheric context, see e.g. Jokipii et al. 1977; Jokipii & Thomas 1981; Burger, Moraal & Webb 1985; Engelbrecht, Mohlolo & Ferreira 2019). GCR drift velocities are calculated following the approach outlined in Burger (2012), where a hyperbolic tangent function is used to model the change in the sign of the AMF over the ACS (see Section 2.2). Due to the unknown nature of the turbulence conditions within the astrospheres, the drift coefficient is assumed to be in the weak-scattering limit. The drift coefficient thus has a maximum value given by the weak-scattering value (Forman, Jokipii & Owens 1974)

$$\kappa_A = \frac{v R_L}{3}. \quad (10)$$

It should be noted that in the presence of turbulence, a reduction factor that depends on turbulence quantities like the magnetic variance should be included (see Minnie et al. 2007; Engelbrecht et al. 2017, and references within), but this is not considered in this study, as the magnetic variances as modelled here (see the next subsection) are generally lower than what is observed in the heliosphere, and it is hence assumed that they would have considerably less of an effect on the drift coefficients. This assumption, however, warrants further investigation in a future study.

2.2 Astrospheric versus heliospheric plasma quantities

A common factor among MHD simulations for astrospheres is that within the TS the stellar wind (SW) speed remains relatively constant as function of radial distance and the AMF can be described as a Parker field as is done for the HMF. This allows for relatively simple analytical descriptions of the SW and AMF that have long been used in the heliosphere. Furthermore, using an analytical description allows for extensive parameter studies. A parameter study requiring MHD runs as input for each parameter change would be prohibitively computationally expensive.

When shifting from heliospheric conditions to the various conditions associated with each unique astrosphere, some assumptions need to be made regarding the large scale plasma parameters that are required to describe the transport coefficients. MHD simulations of various astrospheres (see Baalmann et al. 2021; Meyer et al. 2021; Opher et al. 2021; Herbst et al. 2022) show that the resulting spatial behaviour of the computed AMF within the TS closely resembles that of a Parker (1958) HMF model. It is, therefore, assumed that the AMF can be described using a Parker field and given is by

$$B(r, \theta) = AB_0 \left(\frac{r_0}{r} \right)^2 (\hat{r} - \tan \Psi \hat{\phi}), \quad (11)$$

where the value of B_0 is a normalization value, which is set as the magnitude of the AMF at $r_0 = 1$ au for the various astrospheres. It is also speculatively assumed that the polarity of the AMF behaves similarly to the polarity of the HMF, in that it has a cyclic behaviour and is given by the sign of A . This would imply that when $A > 0$, the magnetic field in the northern hemisphere points away from the star, while the field in the southern hemisphere points towards the star. This effect is flipped for $A < 0$. The angle between the AMF and the radial direction is defined as Ψ and on cones of constant colatitude θ , the AMF displays a spiral structure, where the winding angle is given by

$$\tan \Psi = \frac{\Omega(r - r_s) \sin \theta}{V_{sw}}, \quad (12)$$

which is dependent on the stellar wind speed of the star, V_{sw} , and the stellar rotation rate, Ω . As a first approach it is also assumed that the field source surface of stars is located at $r_s = 0.005$ au, as for the HMF. This assumes that the exoplanets lie outside of the Alfvén surface of the star, which is the case for Proxima Centauri and the exoplanet Proxima Centauri b (see Klein et al. 2021a). The orbit of Prox Cen b is found to be outside of the Alfvén surface of Prox Cen from the MHD simulations of Kavanagh et al. (2021), who also imposes a limit on the required mass-loss rate for the orbit to be inside the Alfvén surface. Following the MHD simulations presented by Herbst et al. (2020b), a radially constant V_{sw} is also assumed within the TS, although this may not necessarily be the case (see e.g. Alvarado-Gómez et al. 2020; Garraffo et al. 2022). An ACS is also included in a similar manner to what is done for heliospheric GCR modulation studies, where the ACS angle is given by (Kota & Jokipii 1983),

$$\theta_{ns} = \frac{\pi}{2} - \tan^{-1} \left[\tan \alpha \sin \left(\frac{\Omega r}{V_{sw}} \right) \right]. \quad (13)$$

The stellar tilt angle between the rotational and magnetic axis of the star is denoted by α . As a first approach, this study assumes a zero tilt angle, leading to a flat current sheet. A tilt angle of 51° will also be considered for Proxima Centauri as has been reported during the activity maximum of that star, motivated by observations reported by (Klein et al. 2021a). Stellar tilt angles for other stars have also been determined from Zeeman-Doppler imaging (e.g. Vidotto et al. 2023), such as 15.5° found for GJ436 (see Bellotti et al. 2023), which has not been considered in this study and 19° for au Microscopii (see Klein et al. 2021b). For more in-depth discussions on the effects of drift in the heliosphere, the reader is invited to consult, e.g. Jokipii & Thomas (1981), Burger et al. (1985), Engelbrecht et al. (2019), Mohlolo et al. (2022), Raath, Ferreira & Kopp (2022), and Troskie, Engelbrecht & Steyn (2024).

The magnetic variance and slab/2D correlation scales are scaled similar to the approach taken by Engelbrecht et al. (2024), by using

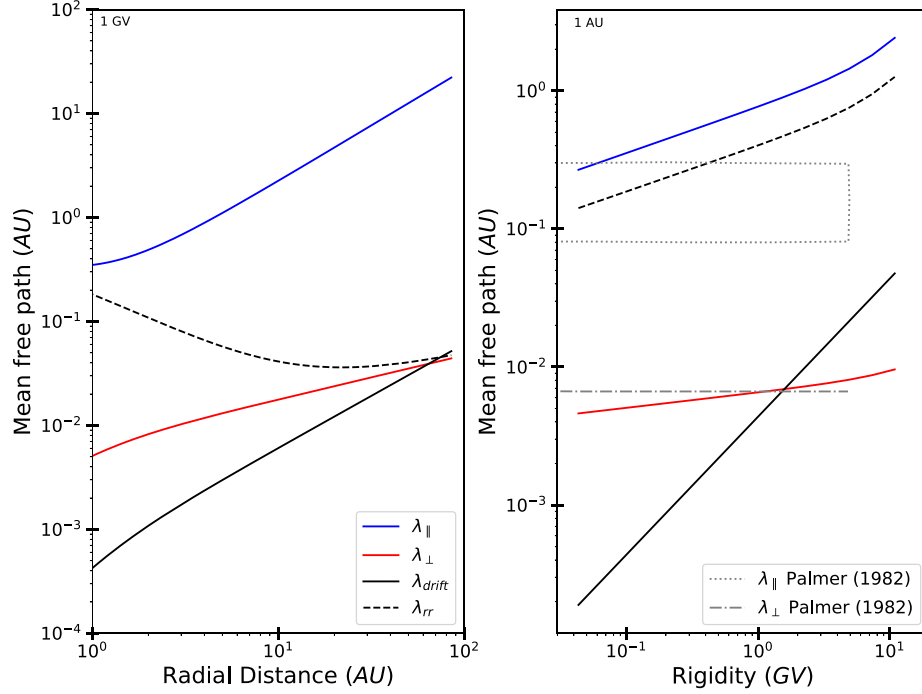


Figure 1. Left panel: Parallel (black), perpendicular (red), drift scale (blue) and radial (dashed) MFPs of 1 GV GCR protons as a function of distance within the heliosphere. Right panel: Parallel (black), perpendicular (blue), drift scale (blue) and radial (dashed) MFPs at 1 au of GCR protons as a function of rigidity. The Palmer (1982) consensus range for parallel (grey dotted) and perpendicular (grey dashed) MFP are shown to guide the eye.

$$\delta B_T^2 = 12.5 n T^2 \times \left(\frac{B_A}{B_H} \right) \left(\frac{r}{r_0} \right)^{-2.5} \quad (14)$$

$$\lambda_{2D} = 0.0074 \text{ au} \times \left(\frac{B_H}{B_A} \right) \left(\frac{r}{r_0} \right)^{0.5} \quad (15)$$

$$\lambda_{sl} = 2.65 \lambda_{2D}, \quad (16)$$

where the correlation scales observed at 1 au within the heliosphere as reported by Weygand et al. (2011) are used. Note that $B_H = 5$ nT and B_A denote the heliospheric and astrospheric magnetic magnitudes at 1 au, respectively. The radial dependencies in equations (14) and (15) are chosen following observations reported within the heliosphere (see e.g. Zank, Matthaeus & Smith 1996; Smith et al. 2001; Cuesta et al. 2022; Burger & McKee 2023). The above approach to modelling the radial dependence of turbulence quantities using observationally based power-law scalings has been successfully employed in heliospheric GCR modulation studies (see e.g. Engelbrecht & Wolmarans 2020; Moloto & Engelbrecht 2020).

2.3 Heliospheric modulation

We now demonstrate that the numerical modulation code discussed above yields results comparable with spacecraft observations for heliospheric input parameters. Solar minimum results within the TS of the heliosphere are obtained for a latitudinally varying solar wind speed with $\sim 400 \text{ km.s}^{-1}$ in the equatorial plane and $\sim 800 \text{ km.s}^{-1}$ over the poles, motivated by spacecraft observations (see e.g. McComas et al. 2008). A HMF magnitude of 5 nT is assumed at a distance of 1 au (Cohen et al. 2008; Cliver & Ling 2011). As the modulation only within the TS is considered, the boundary spectrum is placed at 85 au (Webber et al. 2008). The total variance is here assumed to be 12 nT^2 as reported by Smith et al. (2006), with a 80 : 20

ratio between 2D and slab variances, also motivated by spacecraft observations (see e.g. Bieber et al. 1994).

Fig. 1 shows the different MFPs within the heliosphere for 1 GV GCR protons as a function of radial distance (left panel) and at 1 au as a function of rigidity (right panel). The perpendicular diffusion dominated nature of the heliosphere is visible from the radial MFP (dashed), which at larger radial distances follows the behaviour of the perpendicular MFP (red), due to the winding of the HMF: beyond ~ 10 au, the field is essentially azimuthal, and perpendicular GCR transport must occur to transverse it. Hence, even though the parallel MFP becomes very large in the outer heliosphere, it does not greatly affect GCR transport. Note that drift scales only become significant relative to the perpendicular MFP at larger radial distances. The right panel of Fig. 1 also shows the Palmer (1982) consensus range for parallel (grey dotted) and perpendicular (grey dashed) MFP observations at Earth. This range denotes the consensus values for parallel and perpendicular diffusion coefficients at Earth, based on numerical simulation fits of observed solar energetic particle intensities and anisotropies (for more detail, see e.g. Bieber et al. 1994; Engelbrecht et al. 2022b). The parallel MFP remains somewhat above the Palmer range, due to solar minimum input parameters being used, but well within the range of observational estimates for this quantity (see e.g. Lang et al. 2024). Due to the smaller $\sim 45^\circ$ winding angle at 1 au, the radial MFP follows the larger parallel MFP more closely here. The smaller perpendicular MFP falls on the Palmer consensus values, although it should be noted that observational estimates for this quantity also vary considerably (e.g. Engelbrecht et al. 2022b). Fig. 2 shows the computed DIs at 1 au within the inner heliosheath for $A > 0$ (blue), $A < 0$ (red) and a no drift (dashed) solutions. The computed DIs agree reasonably well with observational data (McDonald et al. 1992) for both $A > 0$ (blue and black dots) and $A < 0$ (red and black crosses). It should be

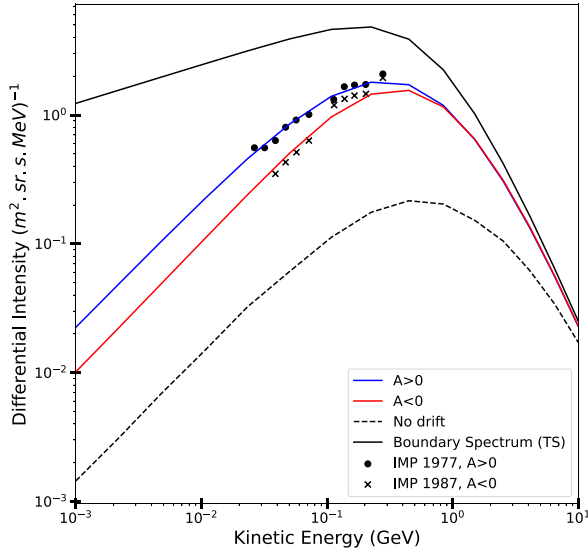


Figure 2. Computed differential intensities at 1 au in the heliosphere for $A > 0$ (blue), $A < 0$ (red) HMF polarity and a no drift solution (dashed). The boundary spectrum (black) of Moloto & Engelbrecht (2020) is placed at the 85 au. Observational data are taken from McDonald et al. (1992) for $A > 0$ (black dots) and $A < 0$ (black crosses), to guide the eye.

noted that tilt angles of 15° and 5° are assumed for $A > 0$ and $A < 0$, respectively, based on observations (see Cliver & Ling 2001). It also shows the expected relation with higher intensities during $A > 0$ and lower intensities during $A < 0$, while drift plays a large role, as indicated by the considerably lower DIs computed when drift effects are switched off (dashed) (see e.g. Engelbrecht & Burger 2015; Moloto et al. 2018; Moloto & Engelbrecht 2020; Mohlolo et al. 2022).

3 SELECTED ASTROSPHERES

The large scale plasma quantities and stellar parameters that are required to model the GCR intensities at the location of the exoplanets are the stellar wind speed of the star, the AMF magnitude, specifically at 1 au, for scaling purposes of the turbulence quantities as discussed in Section 2.2, the location of the exoplanet, the location of the TS (which is where the boundary spectrum will be placed), and the rotation rate of the star. In what follows, the choices made here for these quantities will be motivated on the basis of either observations, or, when these are not available, the results of previously published MHD simulations. For ease of reference, Table 1 shows the parameters used for the calculation of GCR intensities at the exoplanet locations of the astrospheres considered in this work. These values will be motivated below.

3.1 Proxima Centauri

Proxima Centauri (Prox Cen) hosts one confirmed exoplanet within the habitable zone (HZ), namely Proxima Centauri b (hereafter Prox Cen b) (Anglada-Escudé et al. 2016). Prox Cen is a flaring M5.5 dwarf star, which is 1.3 pc from Earth with a stellar mass of $0.122 M_\odot$ and a radius of $0.154 R_\odot$ (Anglada-Escudé et al. 2016). The rocky exoplanet Prox Cen b has a semi-major axis of 0.0485 au with a period of 11 d, while the mass is similar to Earth with a minimum mass of 1.17 Earth masses (Suárez Mascareño et al. 2020). The equilibrium temperature of Prox Cen b is 234 K, which is only

slightly cooler than that of Earth at 255 K (Anglada-Escudé et al. 2016). Flaring activity has been observed from Prox Cen (Vida et al. 2019), while two candidates for coronal mass ejections have been investigated (Moschou et al. 2019; Zic et al. 2020) and coronal dimming has been confirmed (Veronig et al. 2021). A stellar cycle of ~ 7 years was reported by Wargelin et al. (2017) and Klein et al. (2021a). Although stellar cycles have also been observed for other stars, specifically Sun-like stars (see e.g. Jeffers et al. 2022) and M dwarfs (see e.g. Irving et al. 2023), the influence of such cyclical behaviours in stellar plasma parameters are not considered in this work, but will be considered in a future study. For a review on stellar activity cycles, see Jeffers, Kiefer & Metcalfe (2023).

The stellar wind speed of Prox Cen is here assumed to be 1500 km.s^{-1} obtained through simulations (Alvarado-Gómez et al. 2020) and within range of other works (e.g. Herbst et al. 2020b; Garraffo et al. 2022; Peña-Moñino et al. 2024) with an assumed surface magnetic field strength of 600 G (Reiners & Basri 2008; Klein et al. 2021a). Under the assumption that the AMF of Prox Cen behaves similar to the HMF, the magnetic field strength of Prox Cen is here assumed to be 2.4 nT at 1 au (Engelbrecht et al. 2024). This is used with the heliospheric value of the HMF at 1 au, 5 nT, to scale the turbulence quantities. The rotation period for Prox Cen has been measured to be in the range of ~ 82.6 d (Collins, Jones & Barnes 2017) to ~ 89.8 d (Klein et al. 2021a). The differential intensities that are calculated are taken at the location of Prox Cen b, at 0.048 au. The boundary spectrum for Prox Cen is placed at 76 au, which is the TS distance as determined through MHD modelling (see Herbst et al. 2020b). Wargelin et al. (2017) report, based on optical, UV, and X-ray observations of Prox Cen, a stellar cycle with a period of 7.1 years for this star. This is in contrast to the ~ 11 year solar cycle (see e.g. Hathaway 2015). A stellar tilt angle of 51° was measured by Klein et al. (2021a) for conditions corresponding to approximately one year after Prox Cen’s stellar maximum. This is also in contrast to the solar tilt angle during solar maximum, which achieves values greater than $\sim 70^\circ$ (see e.g. Hoeksema 1995; Cliver & Ling 2001).² For the purposes of comparison, results from a modulation model run assuming a tilt angle of 51° will also be compared to those for the case where the ACS is flat (with zero tilt).

3.2 TRAPPIST-1

The TRAPPIST-1 system contains seven exoplanets orbiting around the ultra-cool M8 dwarf star, which is located 12 pc from the Sun, with three of these exoplanets orbiting within the HZ (Gillon et al. 2017). TRAPPIST-1 has a stellar mass of $0.089 M_\odot$, a stellar radius of $0.121 R_\odot$ and an effective equilibrium temperature of 2516 K (Van Grootel et al. 2018). TRAPPIST-1 also shows high flaring activity with complex and multi-peaked frequent strong flares (Vida et al. 2017). The seven exoplanets orbiting TRAPPIST-1 have orbits ranging from 0.011 to 0.062 au (Delrez et al. 2018). Although they are so close to the host star, the exoplanets TRAPPIST-1 e (0.029 au), TRAPPIST-1 f (0.038 au), and TRAPPIST g (0.047 au) are located within the HZ of TRAPPIST-1 (Hill et al. 2023). These three exoplanets have been reported to have Earth-like masses with 0.692, 1.039, and 1.321 Earth masses, respectively (Agol et al. 2021).

The stellar wind speed of TRAPPIST-1 has been found through simulations to reach 1400 km.s^{-1} (see e.g. Garraffo et al. 2017; Harbach et al. 2021), while the magnetic field is assumed to be similar

²For heliospheric observations of the tilt angle, see the Wilcox Solar Observatory’s repository at <http://wso.stanford.edu/Tilts.html>.

Table 1. The stellar wind velocity, stellar magnetic field strength at 1 au, exoplanet location at which GCR differential intensities are calculated, TS location at which the boundary spectrum is placed and rotation period of the stars for the four astrospheres considered in this study, as used in the 3D GCR modulation model. See Section 3 for more detail, and source references.

	Proxima Centauri	TRAPPIST-1	GJ 436	LHS 1140
V_{sw}	1500 km.s ⁻¹	1400 km.s ⁻¹	1290 km.s ⁻¹	250 km.s ⁻¹
B_o	2.4 nT	2.4 nT	1.386 nT	0.3 nT
Exoplanet location	0.048 au	0.03 au	0.028 au	0.096 au
TS location	76 au	76 au	363 au	2.4 au
Rotation period	82.6 d	3.3 d	44 d	131 d

to that of Prox Cen based on the upper limit imposed by Reiners & Basri (2008), and consistent with what is used in the simulations of Harbach et al. (2021). The rotation period of TRAPPIST-1 is much faster than Prox Cen and the heliosphere, having been measured at 3.3 d (Luger et al. 2017). Currently, there are no MHD simulations to give the TS distance for TRAPPIST-1; however, as it is very similar to Prox Cen as a first-order estimate, it is here assumed to be located at 76 au, similar to what is used in other studies (Herbst et al. 2024). The GCR proton differential intensities will be calculated at TRAPPIST-1 e, at a distance of 0.03 au.

3.3 GJ 436

GJ 436 is an M2.5 dwarf at a distance of 9.76 pc (Gaia Collaboration 2023), which has an exoplanet, GJ 436 b, orbiting at a distance of 0.028 au (Rosenthal et al. 2021). This exoplanet was observed to have an extended atmosphere due to the interaction with the SW of GJ 436 (dos Santos et al. 2019). GJ 436 b has a mass of 21.72 Earth masses and a radius of 3.85 Earth radii (Maxted et al. 2022). The GCR intensities within this astrosphere were calculated previously at the position of the exoplanet (see e.g. Mesquita et al. 2021; Rodgers-Lee et al. (2023)). These authors used a stellar wind model to determine the stellar wind speed and magnetic field profiles and obtained two different cases for the stellar wind parameters. For their Case B, which will be considered further in this study, they obtained a stellar wind speed of 1290 km.s⁻¹ and an AMF value of $B = 3.85$ nT at 0.6 au. The exoplanet also orbits outside of the Alfvén radius for this case (see Mesquita et al. 2021). The stellar wind speed of GJ 436 was also determined by fitting Ly α observations and found to range from 250 to 460 km.s⁻¹ (see Villarreal D’Angelo et al. 2021). The magnitude of B is extrapolated to a distance of 1 au assuming a $B \sim r^{-2}$ dependence, and a value of $B = 1.386$ nT at 1 au was obtained, as is necessary for input to the transport model. The rotation period of GJ 436 was determined to be 44 d (see Bourrier et al. 2018). Currently, no large scale MHD results showing the TS locations exist for GJ 436. As such, the TS location of 363 au as reported by Mesquita et al. (2021) will be used in this study for this specific astrosphere.

3.4 LHS 1140

LHS 1140 is an M4.5-type main-sequence red dwarf located 12.5 pc (Dittmann et al. 2017). The star has an estimated stellar mass of 0.179 M_⊙ with a stellar radius of 0.214 R_⊙ (Ment et al. 2019) and a stellar rotation rate of 131 d (Dittmann et al. 2017; Lillo-Box et al. 2020). Two confirmed exoplanets are orbiting around LHS 1140. LHS 1140 b is a rocky super-Earth, with a mass of 6.65 Earth masses and a radius of 1.43 Earth radii (Dittmann et al. 2017) which orbits at 0.096 au, within the HZ of LHS 1140 (Lillo-Box et al. 2020). LHS

1140 c has a mass of 1.81 Earth masses and a radius of 1.28 Earth radii (Ment et al. 2019) and orbits at 0.027 au (Lillo-Box et al. 2020). The astrosphere of LHS 1140 is very different to other astrospheres considered thus far, as it is extremely small in size with very low stellar outflow parameters. The stellar wind speed is here assumed to be 250 km.s⁻¹ and a TS distance of 2.4 au was calculated by (Herbst et al. 2020b) with a stellar magnetic field magnitude assumed for LHS 1140 of 0.3 nT at 1 au. The exoplanet, LHS 1140 b, will be the one at which the differential intensities are calculated. Note that most recently, a high-mean-molecular-weight atmosphere (most likely N₂-dominated) was confirmed using the NIRSpec instrument on JWST (Damiano et al. 2024) favouring LHS 1140 b as a potentially habitable water world.

4 RESULTS

The DIs for periods of positive ($A > 0$, blue) and negative ($A < 0$, red) AMF polarity calculated at Prox Cen b, following the approach of Engelbrecht et al. (2024), however only calculating the modulation within the TS of Prox Cen, can be seen in the left panel of Fig. 3 as a function of kinetic energy. Also shown is the assumed boundary spectrum (black line, see Section 2) and typical observations at Earth (McDonald et al. 1992) (black dots and crosses), to guide the eye. The DI for a flat current sheet at Prox Cen b exceeds the intensities observed at Earth by ~ 50 per cent. This is the same as reported by Engelbrecht et al. (2024) for the case of a flat current sheet and in direct contrast to studies using simpler GCR modulation models (Mesquita et al. 2021; Rodgers-Lee, Vidotto & Mesquita 2021). Drift effects increase intensities at lower energies by a factor of ~ 1.5 , as reported by (Engelbrecht et al. 2024). In contrast to what was seen for the heliosphere in Fig. 2, the intensities for $A < 0$ are higher than the intensities for $A > 0$, due to the slow rotation of Prox Cen resulting in an underwound AMF (relative to the winding of the HMF at a given radial distance), especially when a flat current sheet (dashed) is assumed. This leads to parallel diffusion-dominated transport as the AMF is more radial at the location of the exoplanet. The inclusion of a tilt angle of 51° lowers the intensities during $A < 0$ leading to intensities being similar during $A > 0$ and $A < 0$ polarities. This, however, does not imply that drift effects are not present, as these solutions remain above the no drift solution (black dashed line). This appears to be somewhat similar to what is expected from heliospheric modelling and observations of GCR intensities, where drift effects become less important towards solar maximum (see e.g. Ferreira, Potgieter & Heber 2003; Moloto & Engelbrecht 2020; Raath et al. 2022; Moloto et al. 2023, and references therein). The right panel of Fig. 3 shows the parallel, perpendicular and radial MFPs and drift scale for 1 GV GCR protons as a function of radial distance and a tilt angle of 51°. The contrasting relation between intensities for $A > 0$ and $A < 0$ due to the underwound AMF can be seen by the

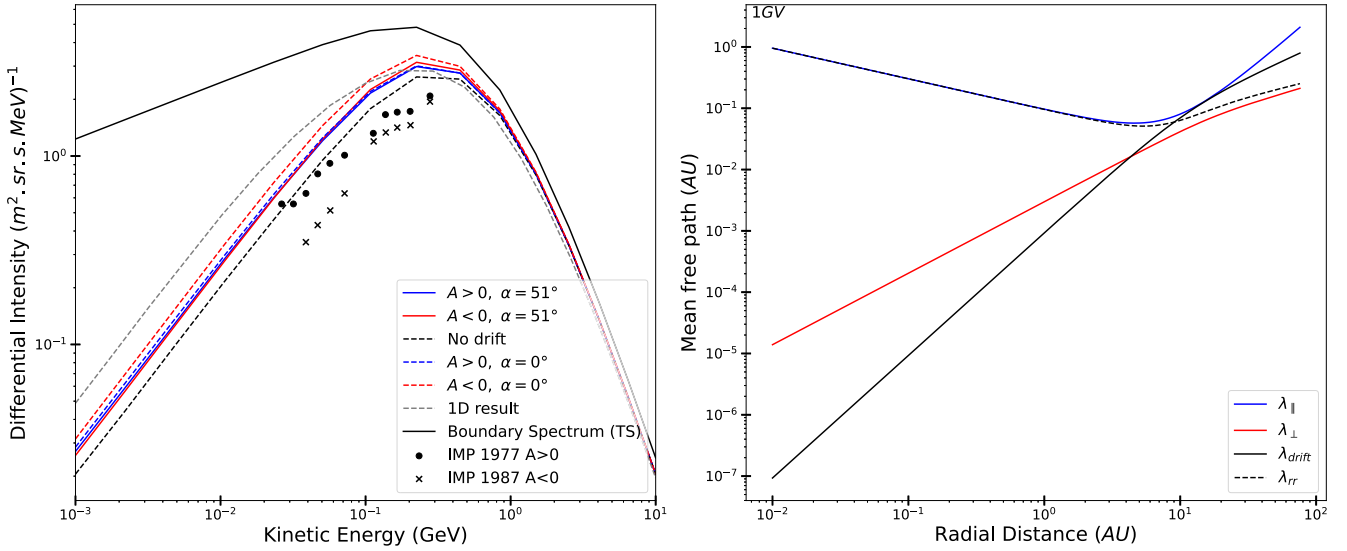


Figure 3. Left panel: Computed differential intensities at Prox Cen b (0.048 au). The differential intensities for $A > 0$ (blue), $A < 0$ (red) AMF polarities, no drift solution (black dashed) are shown. The solid lines show the DI for a tilt angle of 51° , while the dashed lines are for a flat current sheet. The boundary spectrum from Moloto & Engelbrecht (2020) (black) is placed at 76 au. The 1D results using the model from Light et al. (2022) (grey dashed) are also shown. Observational data from McDonald et al. (1992) for $A > 0$ (black dots) and $A < 0$ (black crosses) are shown to guide the eye. Right panel: Calculated parallel MFP (blue), perpendicular MFP (red), drift scale (black), and radial MFP (black dashed) at Prox Cen b (0.048 au) for 1 GV GCR protons and a tilt angle of 51° .

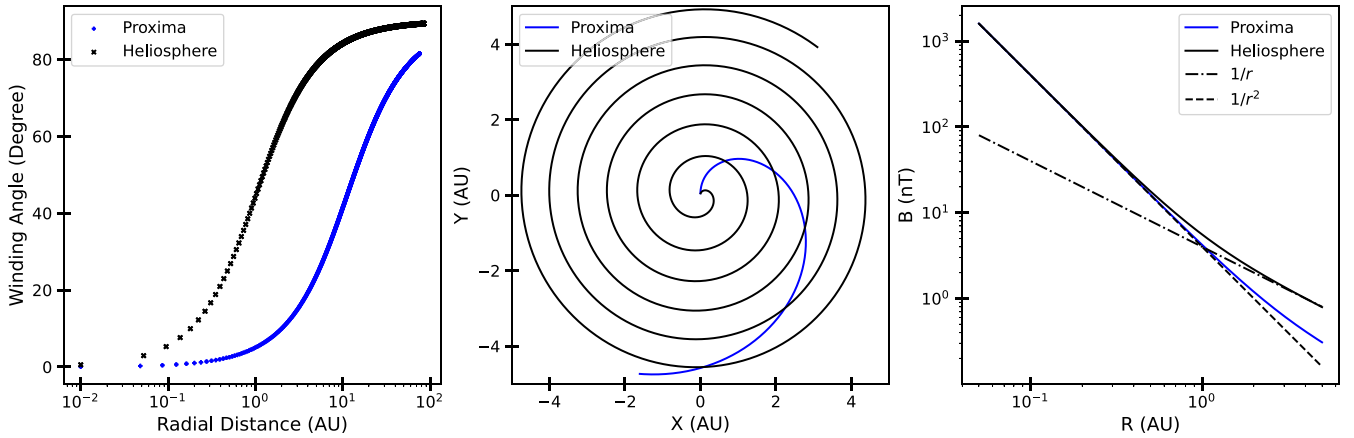


Figure 4. Left panel: Winding angle (equation 12) as a function of radial distance for the heliosphere (black) and Prox Cen (blue). Middle panel: Traces of Parker spirals for the heliosphere (black) and Prox Cen (blue) to a distance of 5 au. Right panel: The magnitude of the Parker magnetic field for the rotation rate of the Sun (solid black) and Prox Cen (blue). A $1/r$ (dashed and dotted) and $1/r^2$ (dashed) dependency is also shown to guide the eye.

radial MFP being dominated by the parallel MFP from the exoplanet location out to a distance of ~ 10 au, after which the perpendicular MFP starts to play a larger role, compared to the heliosphere in Fig. 1, where the radial MFP is pre-dominantly dominated by the perpendicular MFP to distances close to Earth.

The underwound AMF of Prox Cen compared to the HMF can be seen in the left panel of Fig. 4, where a comparison between the winding angle of the HMF and Prox Cen as a function of radial distance as modelled using equation (11) is shown, with each being computed for the differing rotation periods of these stars. The HMF has a winding angle of $\sim 45^\circ$ at 1 au, whereas the AMF of Prox Cen has a winding angle of $\sim 5^\circ$ at a similar distance. The underwound AMF lines within the astrosphere of Prox Cen compared to the HMF

lines can also be seen in the middle panel of Fig. 4, showing a trace of the Parker spirals out to a distance of 5 au. This underwound AMF of Prox Cen also affects the magnetic field magnitude of the AMF, shown in the right panel of Fig. 4. The AMF of Prox Cen has a r^{-2} dependence towards larger radial distances compared to the HMF due to the radial and azimuthal dependence of the magnetic field strength.

The DIs at TRAPPIST-1 e are computed using similar stellar parameters (see Section 3.2) as used by Herbst et al. (2024) and are shown in the left panel of Fig. 5. In contrast to what was seen at Prox Cen b, drift effects play a major role in the modulation of GCR protons, increasing the intensity by ~ 2 orders of magnitude. The relation between higher intensities during $A > 0$ and lower

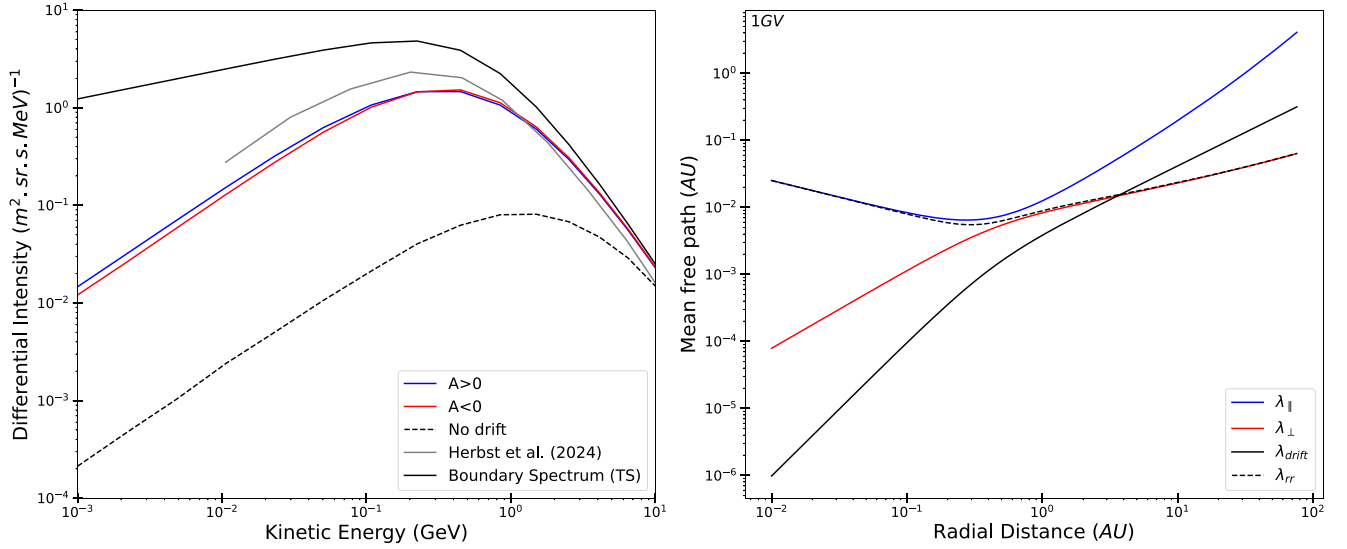


Figure 5. Left panel: Computed differential intensities at TRAPPIST-1 e (0.047 au). The differential intensities shown are similar to Fig. 3, with $A > 0$ (blue), $A < 0$ (red) AMF polarities, no drift solution (black dashed) shown. Results from Herbst et al. (2024) is shown in grey. The boundary spectrum from Moloto & Engelbrecht (2020) (black) is placed at 76 au. Right panel: Calculated parallel MFP (blue), perpendicular MFP (red), drift scale (black), and radial MFP (black dashed) at TRAPPIST-1 e (0.047 au) for 1 GV GCR protons.

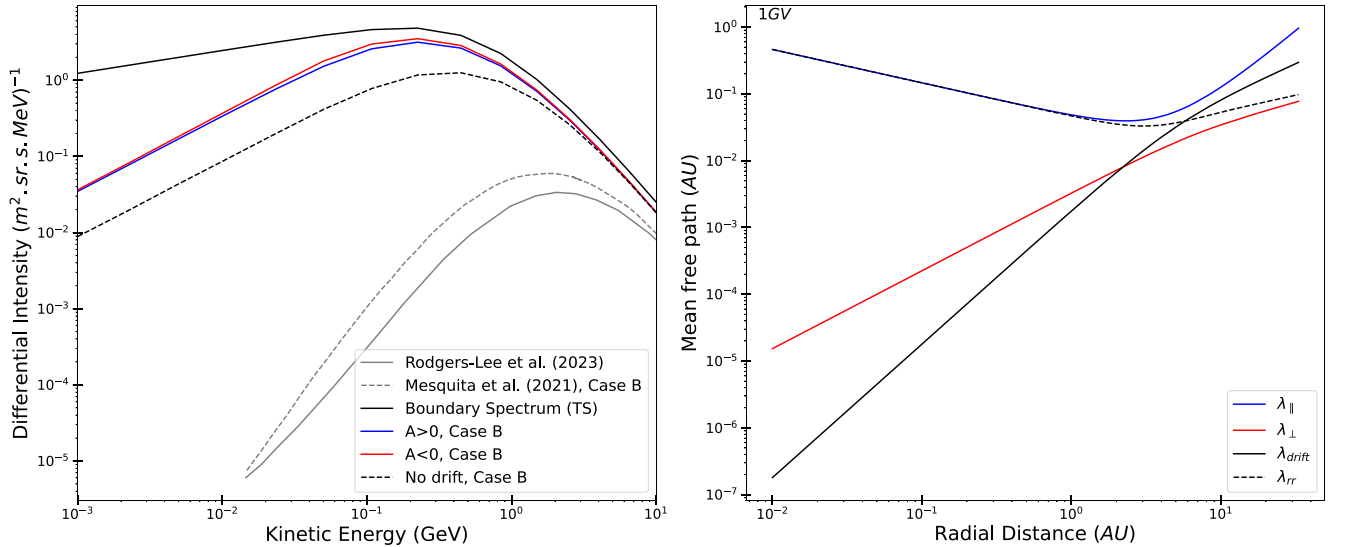


Figure 6. Left panel: Computed differential intensities at GJ 436 b (0.028 au). The differential intensities shown are similar to Fig. 3, with $A > 0$ (blue), $A < 0$ (red) AMF polarities, no drift solution (black dashed) shown. The boundary spectrum from Moloto & Engelbrecht (2020) (black) is placed at 363 au. Results from Mesquita et al. (2021) and Rodgers-Lee et al. (2023) are shown in grey. Right panel: Calculated parallel MFP (blue), perpendicular MFP (red), drift scale (black) and radial MFP (black dashed) at GJ 436 (0.028 au) for 1 GV GCR protons.

intensities during $A < 0$, similar to the heliosphere, can be seen. This is due to the faster rotation rate of TRAPPIST-1, leading to a more tightly wound AMF, thus perpendicular diffusion dominates the transport. The intensities obtained in this study are lower at lower energies and higher at higher energies than intensities reported by Herbst et al. (2024) (grey line). The perpendicular diffusion dominance can also be seen in the radial MFP in the right panel of Fig. 5. Only at small radial distances ($r < 0.2$ au) is the radial MFP dominated by the parallel MFP. The importance of drift in this

case can also be seen by the large drift scale at larger radial distances, where $r > 1.0$ au.

The astrosphere of GJ 436 is considerably larger in this study than those of Prox Cen and TRAPPIST-1, with a TS location at 363 au, but is at the same location as used in other studies (e.g. Mesquita et al. 2021; Rodgers-Lee et al. 2023). Intensities at the location of GJ 436 b for $A > 0$ (blue) and $A < 0$ (red) AMF polarities are shown in the left panel of Fig. 6 with intensities reported by Mesquita et al. (2021) (dashed grey line) and Rodgers-Lee et al. (2023) (solid grey

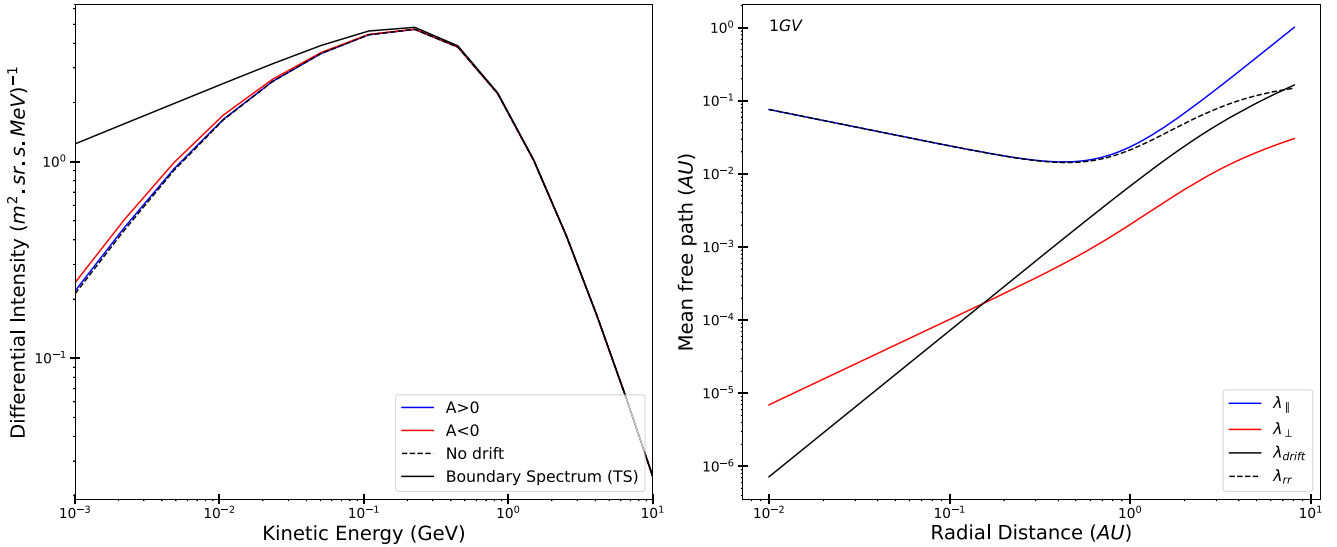


Figure 7. Left panel: Computed differential intensities at LHS 1140 b (0.096 au). The differential intensities shown are similar to Fig. 3, with $A > 0$ (blue), $A < 0$ (red) AMF polarities, no drift solution (black dashed) shown. The boundary spectrum from Moloto & Engelbrecht (2020) (black) is placed at 2.4 au. Right panel: Calculated parallel MFP (blue), perpendicular MFP (red), drift scale (black), and radial MFP (black dashed) at LHS 1140 b (0.096 au) for 1 GV GCR protons.

line) also shown. The results from Rodgers-Lee et al. (2023) use the DI calculated for Case A from Mesquita et al. (2021). Even though the boundary spectrum used in this work is ~ 1 order of magnitude smaller than the LIS employed by Mesquita et al. (2021) at ~ 1 GeV, the intensities calculated in this study are several orders of magnitude (~ 4.5) higher. Drift effects still play a role by increasing the intensities by ~ 50 per cent. The parallel, perpendicular and radial MFP, shown in the right panel of Fig. 6, display behaviour that is similar to what is expected within the heliosphere. This is due to the rotation period of GJ 436, 44 d, being closer to the rotation period of the Sun than any of the other astrospheres.

The DIs for the extremely small astrosphere of LHS 1140, with a TS at a distance of only 2.4 au, are shown in the left panel of Fig. 7. Due to the small size of the astrosphere, at energies above 0.02 GeV there is no modulation visible. Drift does not have an effect on an astrosphere of this size. The long rotation period of the astrosphere also means that transport is parallel diffusion-dominated, as can be seen from the radial MFP in the right panel of Fig. 7.

Each astrosphere considered here has displayed a different relation between positive ($A > 0$) and negative ($A < 0$) polarities of the AMF and the no-drift solutions due to their differing rotation periods. To explore this, Fig. 8 shows the DI at 1 au of 100 MeV GCR protons as a function of rotation period of heliospheric conditions, namely a stellar wind speed of 400 km.s^{-1} , a Parker magnetic field magnitude of 5.0 nT at 1 au, for different boundary spectrum locations. We employ heliospheric conditions as they are well known from spacecraft observations, allowing for the demonstration of the influence of the stellar rotation period on computed GCR intensities with less of the uncertainties implicit to the use of astrospheric plasma input parameters. The boundary spectrum locations shown are for 30 au (dashed lines), 75 au (solid lines), and 120 au (dash-dotted lines). The DI calculated for the rotation period of the Sun, 27 d, is shown by the green star and the DI calculated for the rotation period of Prox Cen, 82.6 d, is shown by the black star. A shorter rotation period leads to a more tightly wound AMF and a decrease in the DI due to particles relying more on diffusion perpendicular to the AMF to reach their

destination as the AMF becomes more azimuthal. As the coefficients for perpendicular transport are smaller than for parallel (see Fig. 1), the intensities decrease with decreasing rotation period. There is a transition point where intensities during negative ($A < 0$) polarities of the AMF are higher than for positive ($A > 0$) polarity. Faster rotation rates produce a more tightly wound AMF that will increase the influence of gradient and curvature drifts compared to current sheet drift, thus intensities for $A > 0$ are higher than for $A < 0$. The transition point where intensities for $A > 0$ are lower than for $A < 0$ occurs at lower rotation periods for a smaller modulation volume, as it occurs at ~ 25 d for a boundary spectrum at 30 au, while for a boundary spectrum at 75 au, the transition occurs at a rotation period of ~ 50 d. This transition moves to ~ 60 d for a boundary spectrum at 120 au.

5 INFLUENCE OF ROTATION PERIOD ON ATMOSPHERIC IONIZATION AND DOSIMETRY

To investigate the impact of the rotation-rate-induced CR intensity changes on planetary objects, here – as a zero-order approximation – we study the Sun under rotation periods between 5 and 150 d and the CR-induced impact upon modern Earth ($\text{N}_2\text{--O}_2$ dominated atmosphere) and modern Mars (thin CO_2 -dominated atmosphere).

One of the primary indicators for the impact of CRs in an atmosphere is changes in the atmospheric ionization profile. The Atmospheric Radiation Interaction Simulator (AtRIS, see Banjac, Herbst & Heber 2019a) is used to compute the ionization and absorbed dose rates. AtRIS has been validated for Earth (e.g. Banjac et al. 2019a; Banjac et al. 2019b; Winant et al. 2023), Mars (e.g. Guo et al. 2019), and Venus (Herbst, Banjac & Nordheim 2019a; Herbst et al. 2020a). Thereby, the induced atmospheric ionization – also referred to as the ion pair production rate – Q is given as

$$Q(E_c, x) = \sum_i \int_{E_c}^{\infty} J_i(E) \cdot Y_i(E, x) dE, \quad (17)$$

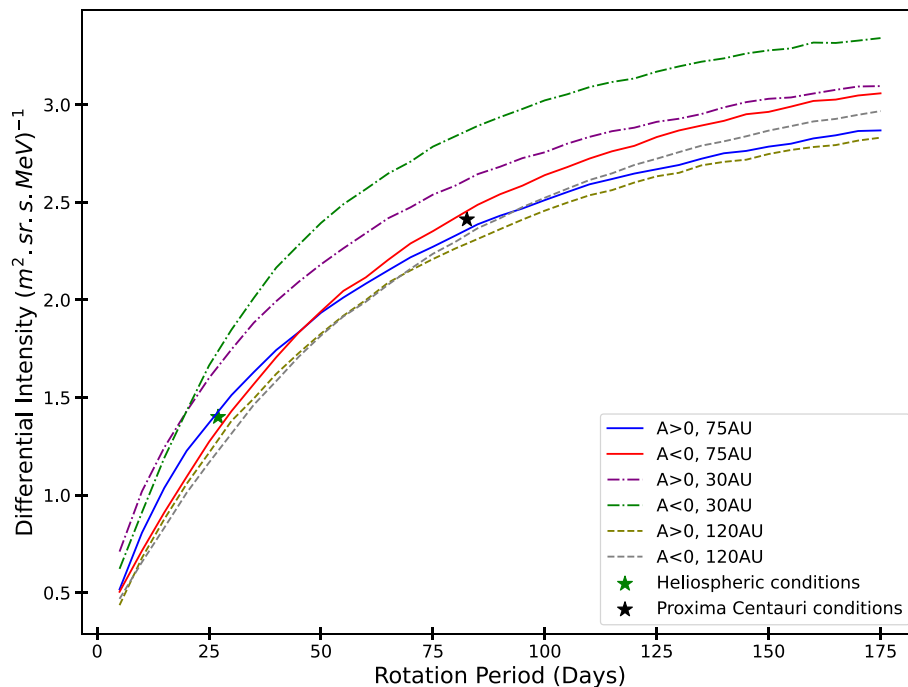


Figure 8. Computed differential intensities of 100 MeV GCR protons as a function of rotation period at different boundary positions, namely 75 au (solid lines), 30 au (dash-dotted), and 120 au (dashed). The intensities for positive ($A > 0$) and negative ($A < 0$) AMF polarities are shown. The rotation period of the Sun (27 d, green star) and Prox Cen (82.6 d, black star) are shown to guide the eye.

where \sum_i is the sum over all primary particles of type i and E_c refers to the so-called cut-off energy, the energy a particle needs to reach a certain location at a certain altitude. In this study, we investigate the impact on regions where the cut-off energy is in the order of 10 MeV. Such low cut-off energies reflect regions with low magnetic shielding (i.e. polar regions at Earth), allowing almost all particles to pass the magnetic field. Thus, such regions are more sensitive to the low-energy part of the cosmic ray flux, and with that more favourable for studying the impact of changing GCR fluxes caused by rotation rate changes.

Further, x refers to the altitude, i to the primary particle type (i.e. protons), and $J_i(E)$ to the differential CR intensity. The ionization yield $Y_i(E, x)$ is given by $2\pi \int \cos(\theta) \sin(\theta) d\theta \cdot \frac{1}{E_{ion}} \frac{\Delta E_i}{\Delta x}$, where E_{ion} is the average atmospheric ionization energy³ and $\frac{\Delta E_i}{\Delta x}$ the mean specific energy loss of a primary particle at a certain altitude.

The rotation-rate dependent GCR-induced ionization rates in an Earth-like and Mars-like atmosphere are shown in the left and right panels of Fig. 9, respectively. Here, the coloured lines reflect the results based on $A > 0$ conditions (i.e. the lighter the colour, the faster the rotation period). In comparison, the black dashed lines correspond to $A < 0$ conditions with rotation periods of 5, 50, 100, and 150 d (from left to right).

Overall, both scenarios show that the longer the stellar rotation period, the higher the altitude-dependent ionization rates. However, the atmosphere of modern Earth is more responsive to the higher GCR fluxes at altitudes above 10 km (up to 100 per cent difference at altitudes above 30 km) while the thin CO₂ dominated atmosphere of modern Mars shows increases of 60 per cent at the surface up to

100 per cent at altitudes above 20 km. Nevertheless, both scenarios show magnetic polarity cycle dependent increases, emphasizing the importance of 3D drift effects. In general, the rotation-period dependent ionization rates are higher during $A < 0$ conditions.

Besides directly providing atmospheric ionization profiles, AtRIS further provides the pre-calculated relative ionization efficiency $\mathcal{I}_{R,j}(E_i)$, that reflects the ratio between the average ionization energy a particle of type j is causing in, e.g. a phantom reflecting the human body⁴ and the energy of the primary particle. This ratio can be used to further study the CR-induced radiation exposure, i.e. in the form of the absorbed dose rates \bar{D}_j . The latter is given by

$$\bar{D}_j(E_i, r) = \mathcal{I}_{R,j}(E_i) \cdot \frac{E_i}{m_{ph}(r)}, \quad (18)$$

where m_{ph} gives the mass of the phantom ($m_{ph} = \rho \cdot \frac{4}{3}\pi \cdot r_{ph}^3$, see e.g. Herbst et al. 2020a). Convolving the results with the primary particle spectrum and summing up over all energy bins and particle types provides the GCR-induced dose rate profiles shown in the panels of Fig. 10. A similar response to the rotation rate-dependent GCR fluxes can be seen: the longer the rotation period, the higher the radiation exposure throughout the atmosphere. However, in contrast to the Earth-like atmosphere, it is only in the case of the thin CO₂-dominated Martian atmosphere (right panel) that significant radiation enhancements of up to 20 per cent can be observed at the planetary surface due to the enhanced stellar rotation period. Thereby, the surface changes are slightly smaller during $A < 0$ conditions.

³In this study, we assume an average atmospheric ionization energy of 32 eV for the N₂-O₂-dominated atmosphere and 28 eV for the thin CO₂-dominated atmosphere (e.g. Simon Wedlund et al. 2011).

⁴To represent and reflect life as we know it from Earth, the International Commission on Radiation Units (ICRU) and Measurements proposed a 15 cm radius tissue-equivalent sphere (i.e. ICRU sphere) with a density of 1 g cm⁻³ composed of 76.2 per cent oxygen, 11.1 per cent carbon, 10.1 per cent hydrogen, and 2.6 per cent nitrogen (McNair 1981).

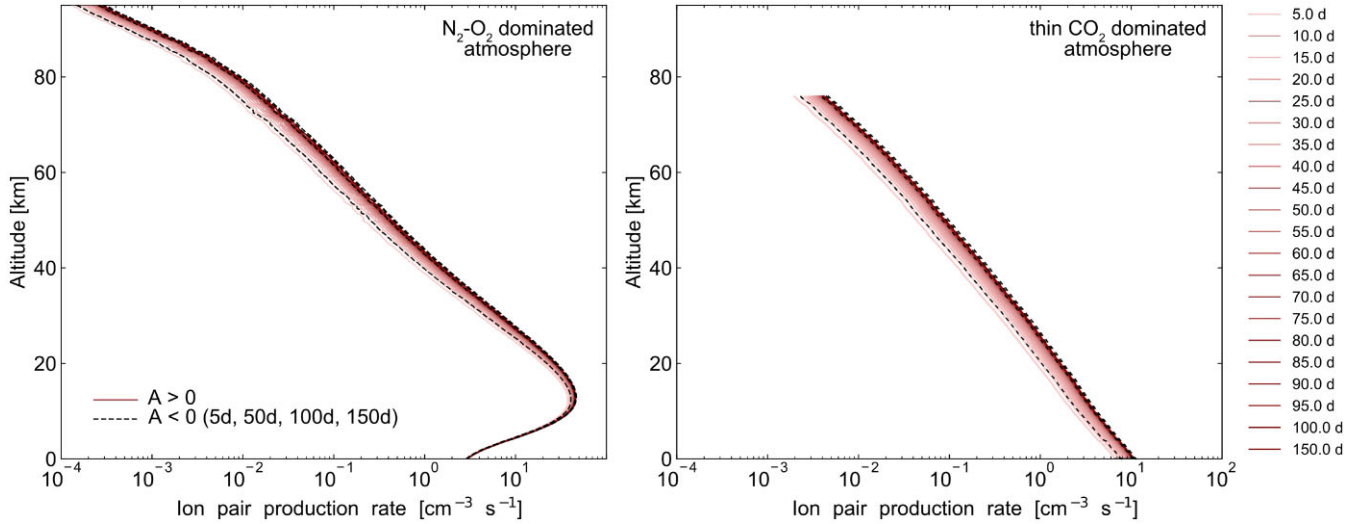


Figure 9. GCR-induced ion pair production rates during $A > 0$ (colored lines) and $A < 0$ (black dashed lines) conditions. Left: Response of a (Earth-like) $\text{N}_2\text{-O}_2$ -dominated atmosphere. Right: Response of a thin (Mars-like) CO_2 -dominated atmosphere. Note that in the case of the black dashed lines (i.e. $A < 0$ conditions), the lowest rates correspond to a rotation period of 5 d, while the highest rates reflect those of the 150-d rotation period scenario.

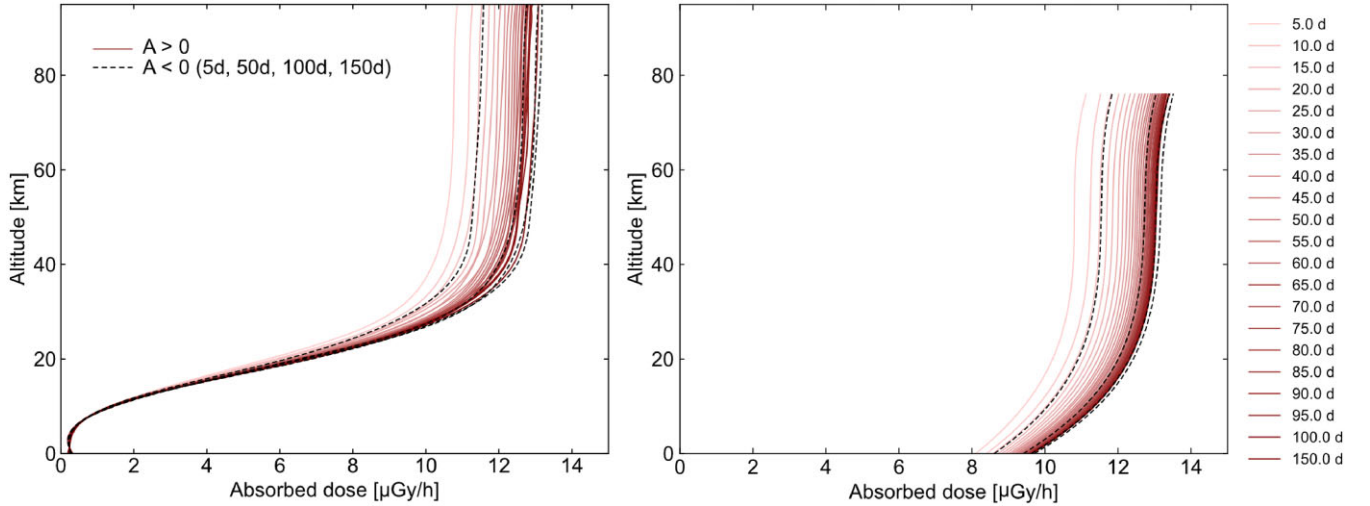


Figure 10. GCR-induced absorbed dose rates during $A > 0$ (coloured lines) and $A < 0$ (black dashed lines) conditions. Left: Response of a (Earth-like) $\text{N}_2\text{-O}_2$ dominated atmosphere. Right: Response of a thin (Mars-like) CO_2 dominated atmosphere.

6 SUMMARY AND DISCUSSION

We present here detailed 3D studies of the transport of GCRs for several exoplanet-hosting astrospheres. These astrospheres, namely those of Prox Cen, TRAPPIST-1, GJ 436, and LHS 1140, were chosen for two reasons. First, sufficient information as to their large-scale plasma properties, such as their stellar winds and AMFs, is available either from observations or MHD simulations to allow for 3D modelling as is done in this study (see Section 3), and secondly, due to their representing very different GCR transport conditions. The present 3D investigation is unique for some of these systems, as the transport of GCRs in some of them has only been considered using 1D models in the past. We demonstrate, via comparisons with the results of those prior studies for TRAPPIST-1 and GJ 436, that a 1D approach can yield results very different from those calculated using the 3D approach presented here, and argue that this is due to the fact that a 1D approach simply cannot take into account inherently 3D transport processes, such as drifts, that are known to play a

significant role in the heliospheric transport of GCRs. In brief, then, the inherently 3D nature of the transport mechanisms influencing the modulation of GCRs throughout the heliosphere and subsequently other astrospheres, sets the requirement for the modelling of these processes three-dimensionally.

The importance of 3D modelling is also demonstrated by this study through the unexpectedly large influence that the rotation rate of a star would have on the transport mechanisms that dominate within the astrospheres. One of the aims of this study is to investigate the significance of the stellar rotation period on GCR intensities at exoplanetary locations, which was shown by Engelbrecht et al. (2024) to be significant for Prox Cen b. A slower rotation rate would imply an underground (relative to the HMF) astrospheric magnetic field, with the implication that the more effective diffusion parallel to the AMF would dominate the radial diffusion coefficient, as opposed to the less effective perpendicular diffusion coefficient, leading to larger GCR intensities. Hence, in the case of the slow (relative to

the Sun) rotating Prox Cen, computed GCR intensities at Prox Cen b are higher than those observed at Earth. For the slow-rotating LHS1140, the computed GCR spectrum is essentially unmodulated, except below ~ 0.01 GeV. This is similar to what was reported by Herbst et al. (2020b), and it should be noted that such a small astrosphere would not be expected to modulate the local interstellar GCR spectrum much. A faster rotation rate (relative to the Sun), like that of TRAPPIST-1, leads to a more wound AMF, resulting in the dominance of perpendicular diffusion and drift environments of exoplanets and hence lower GCR intensities than seen at Earth. This result is emphasized in Fig. 8: the hallmark of large stellar rotation periods is high GCR intensities, combined with a reversal of the usual heliospheric relation between GCR intensities computed for positive and negative magnetic polarities. The opposite can be seen for slow rotation periods. Intriguingly, at a rotation period of somewhat less than ~ 50 d, GCR intensities during $A > 0$ and $A < 0$ are equal, representing a cross-over of these effects.

To study the impact of GCRs on (exo)planetary atmospheres, we further investigated their influence on modern Earth and Mars around the Sun with different rotation periods (i.e. varying between 5 and 150 d, as in Fig. 8) and differing magnetic polarity cycle conditions ($A > 0$ and $A < 0$). Overall, both atmospheres show the same behaviour: The longer the stellar rotation period, the stronger the GCR-induced atmospheric ionization and radiation exposure within. With changes of the order of more than 100 per cent, both atmospheres are strongly affected by the changing GCR flux above an altitude of 30 km. Keeping in mind that the transmission spectra of exoplanets are based on information of the atmospheric chemistry – and with that on biosignatures and transmission features – within these altitudes, this emphasizes the need for more reliable information on the GCR-induced background ionization (and radiation exposure) to interpret future *JWST* and Ariel observations. However, we further show that the atmospheric changes strongly depend on atmospheric composition: While the varying GCR flux primarily impacts the upper terrestrial atmosphere (down to about 10 km), the thin CO_2 -dominated Martian atmosphere shows changes in atmospheric ionization and radiation exposure down to the Martian surface. Thereby, about 20 per cent higher dose rates occur due to the variation of the solar rotation period from 5 to 150 d. However, the presented results do not include the deflecting of GCRs due to a planetary magnetic field (e.g. Herbst et al. 2019b) and hence more sophisticated future investigations are required. Lastly, as noted by Engelbrecht et al. (2024) in their study of stellar energetic particle transport in Proxima Centauri’s astrosphere, the astrospheric magnetic field geometry arising from a slowly rotating star could in principle also provide, through diffusion parallel to the AMF, a highway for these particles into the broader astrosphere. This would increase their intensity and hence their influence on exoplanetary atmospheres. An investigation of this will be the subject of future work.

ACKNOWLEDGEMENTS

The authors gratefully acknowledge the support of Deutsche Forschungsgemeinschaft (DFG) grant *HE 8392/2-1* (project 508335258) to initialize this international collaboration and thank the Center for High Performance Computations (CHPC) in Cape Town for partially funding the project under the project *ASTRO1277*. KH acknowledges the support of the DFG priority program SPP 1992 ‘Exploring the Diversity of Extrasolar Planets (*HE 8392/1-1*)’. This project has received funding from the Research Council of Norway through the Centres of Excellence funding scheme, project number

332523 (PHAB). KS acknowledges the support of the DFG grant *SCHE 334/16-1* (project 491027218). This work is based on the research supported partly by the National Research Foundation of South Africa (NRF grant number 137793). Opinions expressed and conclusions arrived at are those of the authors and are not necessarily to be attributed to the NRF. The authors gratefully acknowledge the Gauss Centre for Supercomputing e.V. (www.gauss-centre.eu) for funding this project by providing computing time through the John von Neumann Institute for Computing (NIC) on the GCS Supercomputer JUWELS at Jülich Supercomputing Centre (JSC).

DATA AVAILABILITY

The data underlying this article are available in the article and in its online supplementary material.

REFERENCES

- Agol E. et al., 2021, *Planet. Sci. J.*, 2, 1
 Alvarado-Gómez J. D., Drake J. J., Garraffo C., Cohen O., Poppenhaeger K., Yadav R. K., Moschou S. P., 2020, *ApJ*, 902, L9
 Anglada-Escudé G. et al., 2016, *Nature*, 536, 437
 Baalman L. R., Scherer K., Kleimann J., Fichtner H., Bomans D. J., Weis K., 2021, *A&A*, 650, A36
 Baalman L. R., Scherer K., Kleimann J., Fichtner H., Bomans D. J., Weis K., 2022, *A&A*, 663, A10
 Banjac S., Heber B., Herbst K., Berger L., Burmeister S., 2019b, *J. Geophys. Res. Space Phys.*, 124, 9774 <https://doi.org/10.1029/2019JA026622>
 Banjac S., Herbst K., Heber B., 2019a, *J. Geophys. Res. Space Phys.*, 124, 50 <https://doi.org/10.1029/2018JA026042>
 Barth P. et al., 2021, *MNRAS*, 502, 6201
 Bellotti S. et al., 2023, *A&A*, 676, A139
 Bieber J. W., Matthaeus W. H., Smith C. W., Wanner W., Kallenrode M.-B., Wibberenz G., 1994, *ApJ*, 420, 294
 Bieber J. W., Wanner W., Matthaeus W. H., 1996, *J. Geophys. Res.*, 101, 2511
 Bourrier V. et al., 2018, *Nature*, 553, 477
 Bruno R., Carbone V., 2013, *Living Rev. Solar Phys.*, 10, 2
 Burger R. A., 2012, *ApJ*, 760, 60
 Burger R. A., Krüger T. P. J., Hitge M., Engelbrecht N. E., 2008, *ApJ*, 674, 511
 Burger R. A., McKee S. R., 2023, *Adv. Space Res.*, 71, 4916
 Burger R. A., Moraal H., Webb G. M., 1985, *Ap&SS*, 116, 107
 Caballero-Lopez R. A., Moraal H., 2004, *J. Geophys. Res.*, 109, A01101
 Cliver E. W., Ling A. G., 2001, *ApJ*, 551, L189
 Cliver E. W., Ling A. G., 2011, *Sol. Phys.*, 274, 285
 Cohen O., Sokolov I. V., Roussev I. I., Gombosi T. I., 2008, *J. Geophys. Res. (Space Phys.)*, 113, A03104
 Collins J. M., Jones H. R. A., Barnes J. R., 2017, *A&A*, 602, A48
 Cuesta M. E., Parashar T. N., Chhiber R., Matthaeus W. H., 2022, *ApJS*, 259, 23
 Damiano M., Bello-Arufe A., Yang J., Hu R., 2024, *ApJL*, 968, L22, 10.3847/2041-8213/ad5204
 Delrez L. et al., 2018, *MNRAS*, 475, 3577
 Dittmann J. A. et al., 2017, *Nature*, 544, 333
 dos Santos L. A. et al., 2019, *A&A*, 629, A47
 Engelbrecht N. E., Wolmarans C. P., 2020, *Adv. Space Res.*, 66, 2722
 Engelbrecht N. E. et al., 2022a, *Space Sci. Rev.*, 218, 33
 Engelbrecht N. E., 2019, *ApJ*, 872, 124
 Engelbrecht N. E., Burger R. A., 2015, *ApJ*, 814, 152
 Engelbrecht N. E., Di Felice V., 2020, *Phys. Rev. D*, 102, 103007
 Engelbrecht N. E., Herbst K., Strauss R. D. T., Scherer K., Light J., Moloto K. D., 2024, *ApJ*, 964, 89
 Engelbrecht N. E., Mohlolo S. T., Ferreira S. E. S., 2019, *ApJ*, 884, L54
 Engelbrecht N. E., Moloto K. D., 2021, *ApJ*, 908, 167
 Engelbrecht N. E., Strauss R. D., le Roux J. A., Burger R. A., 2017, *ApJ*, 841, 107

- Engelbrecht N. E., Vogt A., Herbst K., Du Toit Strauss R., Burger R. A., 2022b, *ApJ*, 929, 8
- Ferreira S., Potgieter M., Heber B., 2003, *Adv. Space Res.*, 32, 645 [https://doi.org/10.1016/S0273-1177\(03\)00350-8](https://doi.org/10.1016/S0273-1177(03)00350-8)
- Forman M. A., Jokipii J. R., Owens A. J., 1974, *ApJ*, 192, 535
- Forsyth R. J., Horbury T. S., Balogh A., Smith E. J., 1996, *Geophys. Res. Lett.*, 23, 595
- Frisch U., 1995, *Turbulence: The legacy of A.N. Kolmogorov*, Cambridge University Press, Cambridge
- Gaia Collaboration, 2023, *A&A*, 674, A1
- Gardner J. P. et al., 2006, *Space Sci. Rev.*, 123, 485
- Gardner J. P. et al., 2023, *PASP*, 135, 068001
- Garraffo C., Alvarado-Gómez J. D., Cohen O., Drake J. J., 2022, *ApJ*, 941, L8
- Garraffo C., Drake J. J., Cohen O., Alvarado-Gómez J. D., Moschou S. P., 2017, *ApJ*, 843, L33
- Gillon M. et al., 2017, *Nature*, 542, 456
- Gleeson L. J., Axford W. I., 1968, *ApJ*, 154, 1011
- Globus N., Blandford R. D., 2020, *ApJ*, 895, L11
- Guo J., Banjac S., Röstel L., Terasa J. C., Herbst K., Heber B., Wimmer-Schweingruber R. F., 2019, *J. Space Weather Space Clim.*, 9, A2
- Harbach L. M., Moschou S. P., Garraffo C., Drake J. J., Alvarado-Gómez J. D., Cohen O., Fraschetti F., 2021, *ApJ*, 913, 130
- Hathaway D. H., 2015, *Living Rev. Solar Phys.*, 12, 4
- Herbst K. et al., 2019b, *A&A*, 631, A101
- Herbst K. et al., 2020b, *ApJ*, 897, L27
- Herbst K. et al., 2022, *Space Sci. Rev.*, 218, 29
- Herbst K. et al., 2024, *ApJ*, 961, 164
- Herbst K., Banjac S., Atri D., Nordheim T. A., 2020a, *A&A*, 633, A15
- Herbst K., Banjac S., Nordheim T. A., 2019a, *A&A*, 624, A124
- Hill M. L., Bott K., Dalba P. A., Fetherolf T., Kane S. R., Kopparapu R., Li Z., Ostberg C., 2023, *AJ*, 165, 34
- Hoeksema J. T., 1995, *Space Sci. Rev.*, 72, 137
- Irving Z. A., Saar S. H., Wargelin B. J., do Nascimento J.-D., 2023, *ApJ*, 949, 51
- Jeffers S. V. et al., 2022, *A&A*, 661, A152
- Jeffers S. V., Kiefer R., Metcalfe T. S., 2023, *Space Sci. Rev.*, 219, 54
- Jokipii J. R., 1966, *ApJ*, 146, 480
- Jokipii J. R., Levy E. H., Hubbard W. B., 1977, *ApJ*, 213, 861
- Jokipii J. R., Thomas B., 1981, *ApJ*, 243, 1115
- Kavanagh R. D., Vidotto A. A., Klein B., Jardine M. M., Donati J.-F., Ó Fionnagáin D., 2021, *MNRAS*, 504, 1511
- Kennedy A. R., 2014, *Life Sci. Space Res.*, 1, 10 <https://doi.org/10.1016/j.lsr.2014.02.004>
- Klein B. et al., 2021b, *MNRAS*, 502, 188
- Klein B., Donati J.-F., Hébrard É. M., Zaire B., Folsom C. P., Morin J., Delfosse X., Bonfils X., 2021a, *MNRAS*, 500, 1844
- Kolmogorov A., 1941, *Akademiia Nauk SSSR Doklady*, 30, 301
- Kota J., Jokipii J. R., 1983, *ApJ*, 265, 573
- Lang J. T., Strauss R. D., Engelbrecht N. E., van den Berg J. P., Dresing N., Ruffolo D., Bandyopadhyay R., 2024, *ApJ*, 971, 105
- Light J., Ferreira S. E. S., Engelbrecht N. E., Scherer K., Herbst K., 2022, *MNRAS*, 516, 3284
- Lillo-Box J. et al., 2020, *A&A*, 642, A121
- Luger R. et al., 2017, *Nat. Astron.*, 1, 0129
- Mackey J., Green S., Moutzouri M., 2020, *Journal of Physics: Conference Series*, 012012, 1742-6588
- Matthaeus W. H., Bieber J. W., Ruffolo D., Chuychai P., Minnie J., 2007, *ApJ*, 667, 956
- Matthaeus W. H., Goldstein M. L., 1982, *J. Geophys. Res.*, 87, 6011
- Matthaeus W. H., Goldstein M. L., Roberts D. A., 1990, *J. Geophys. Res.*, 95, 20673
- Matthaeus W. H., Qin G., Bieber J. W., Zank G. P., 2003, *ApJ*, 590, L53
- Maxted P. F. L. et al., 2022, *MNRAS*, 514, 77
- McComas D. J., Ebert R. W., Elliott H. A., Goldstein B. E., Gosling J. T., Schwadron N. A., Skoug R. M., 2008, *Geophys. Res. Lett.*, 35, L18103
- McDonald F. B., Moraal H., Reinecke J. P. L., Lal N., McGuire R. E., 1992, *J. Geophys. Res.*, 97, 1557
- McNair A., 1981, *J. Labelled Compounds Radiopharmaceuticals*, 18, 1398
- Ment K. et al., 2019, *AJ*, 157, 32
- Mesquita A. L., Rodgers-Lee D., Vidotto A. A., 2021, *MNRAS*, 505, 1817
- Mesquita A. L., Rodgers-Lee D., Vidotto A. A., Atri D., Wood B. E., 2022, *MNRAS*, 509, 2091
- Meyer D. M. A., Mignone A., Petrov M., Scherer K., Velázquez P. F., Boumis P., 2021, *MNRAS*, 506, 5170
- Minnie J., Bieber J. W., Matthaeus W. H., Burger R. A., 2007, *ApJ*, 670, 1149
- Mohlolo S. T., Engelbrecht N. E., Ferreira S. E. S., 2022, *Adv. Space Res.*, 69, 2574
- Moloto K. D., Engelbrecht N. E., 2020, *ApJ*, 894, 121
- Moloto K. D., Engelbrecht N. E., Burger R. A., 2018, *ApJ*, 859, 107
- Moloto K. D., Engelbrecht N. E., Strauss R. D., Moeketsi D. M., van den Berg J. P., 2019, *Adv. Space Res.*, 63, 626
- Moloto K. D., Eugene Engelbrecht N., Strauss R. D., Diedericks C., 2023, *Adv. Space Res.*, 72, 830
- Moraal H., 2013, *Space Sci. Rev.*, 176, 299
- Moschou S.-P., Drake J. J., Cohen O., Alvarado-Gómez J. D., Garraffo C., Fraschetti F., 2019, *ApJ*, 877, 105
- Opher M. et al., 2021, *ApJ*, 922, 181
- Oughton S., Engelbrecht N. E., 2021, *New Astron.*, 83, 101507
- Oughton S., Matthaeus W. H., Wan M., Osman K. T., 2015, *Phil. Trans. R. Soc. London Ser. A*, 373, 20140152
- Palmer I. D., 1982, *Rev. Geophys. Space Phys.*, 20, 335
- Parker E. N., 1958, *ApJ*, 128, 664
- Parker E. N., 1965, *Planet. Space Sci.*, 13, 9
- Pei C., Bieber J. W., Burger R. A., Clem J., 2010, *J. Geophys. Res. (Space Phys.)*, 115, A12107
- Peña-Moñino L., Pérez-Torres M., Varela J., Zarka P., 2024, *A&A*, 688, A138
- Potgieter M. S., 2013, *Living Rev. Solar Phys.*, 10, 3
- Potgieter M. S., Burger R. A., 1990, *A&A*, 233, 598
- Raath J. L., Ferreira S. E. S., Kopp A., 2022, *A&A*, 665, A4
- Reinecke J. P. L., Potgieter M. S., 1994, *J. Geophys. Res.*, 99, 14761
- Reiners A., Basri G., 2008, *A&A*, 489, L45
- Rimmer P. B., Helling C., Bilger C., 2014, *Int. J. Astrobiol.*, 13, 173
- Rodgers-Lee D. et al., 2023, *MNRAS*, 521, 5880
- Rodgers-Lee D., Vidotto A. A., Mesquita A. L., 2021, *MNRAS*, 508, 4696
- Rogers T. M., Showman A. P., 2014, *ApJ*, 782, L4
- Rosenthal L. J. et al., 2021, *ApJS*, 255, 8
- Sadovskii A. M., Struminsky A. B., Belov A., 2018, *Astron. Lett.*, 44, 324
- Shalchi A., 2009, *Nonlinear Cosmic Ray Diffusion Theories*. Astrophysics and Space Science Library Vol. 362. Springer, Berlin
- Shalchi A., 2020, *ApJ*, 898, 135
- Shalchi A., Bieber J. W., Matthaeus W. H., 2004, *ApJ*, 604, 675
- Simon Wedlund C., Gronoff G., Liliensten J., Ménager H., Barthélemy M., 2011, *Ann. Geophys.*, 29, 187
- Smith C. W., Isenberg P. A., Matthaeus W. H., Richardson J. D., 2006, *ApJ*, 638, 508
- Smith C. W., Matthaeus W. H., Zank G. P., Ness N. F., Oughton S., Richardson J. D., 2001, *J. Geophys. Res.*, 106, 8253
- Stone E. C., Cummings A. C., McDonald F. B., Heikkilä B. C., Lal N., Webber W. R., 2013, *Science*, 341, 150
- Strauss R. D. T., Effenberger F., 2017, *Space Sci. Rev.*, 212, 151
- Strauss R. D., Potgieter M. S., Kopp A., Büsching I., 2011, *J. Geophys. Res. (Space Phys.)*, 116, A12105
- Suárez Mascareño A. et al., 2020, *A&A*, 639, A77
- Teufel A., Schlickeiser R., 2003, *A&A*, 397, 15
- Tinetti G., Eccleston P., Lueftinger T., Salvignol J.-C., Fahmy S., Alves de Oliveira C., and the Ariel team. 2022, Ariel: Enabling planetary science across light-years, Eur. Planet. Sci. Congr. EPSC2022–1114,
- Troskie J. S., Engelbrecht N. E., Steyn P. J., 2024, *ApJ*, 970, 144
- Van Grootel V. et al., 2018, *ApJ*, 853, 30
- Veronig A. M., Odert P., Leitzinger M., Dissauer K., Fleck N. C., Hudson H. S., 2021, *Nat. Astron.*, 5, 697
- Vida K., Kővári Z., Pál A., Oláh K., Kriskovics L., 2017, *ApJ*, 841, 124
- Vida K., Oláh K., Kővári Z., van Driel-Gesztelyi L., Moór A., Pál A., 2019, *ApJ*, 884, 160

- Vidotto A. A., Bourrier V., Fares R., Bellotti S., Donati J. F., Petit P., Hussain G. A. J., Morin J., 2023, *A&A*, 678, A152
- Vidotto A. A., Jardine M., Opher M., Donati J. F., Gombosi T. I., 2011, *MNRAS*, 412, 351
- Villarreal D'Angelo C., Vidotto A. A., Esquivel A., Hazra G., Youngblood A., 2021, *MNRAS*, 501, 4383
- Wargelin B. J., Saar S. H., Pojmański G., Drake J. J., Kashyap V. L., 2017, *MNRAS*, 464, 3281
- Webber W. R., Cummings A. C., McDonald F. B., Stone E. C., Heikkilä B., Lal N., 2008, *J. Geophys. Res. (Space Phys.)*, 113, A10108
- Weygand J. M., Matthaeus W. H., Dasso S., Kivelson M. G., 2011, *J. Geophys. Res. (Space Phys.)*, 116, A08102
- Winant A., Pierrard V., Botek E., Herbst K., 2023, *Universe*, 9 502
- Zank G. P., Matthaeus W. H., Smith C. W., 1996, *J. Geophys. Res.*, 101, 17093
- Zhang M., 1999, *ApJ*, 513, 409
- Zic A. et al., 2020, *ApJ*, 905, 23

This paper has been typeset from a \LaTeX file prepared by the author.